RSC Advances

ROYAL SOCIETY OF CHEMISTRY

www.rsc.org/advances

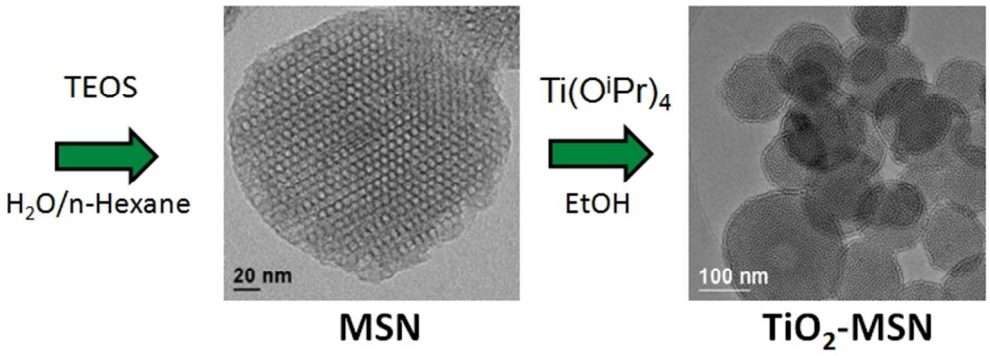

Titania nanoparticles were confined inside the pore channels of preformed mesoporous silica nanoparticles MSN for the photodegradation of dyes and drugs.

Cite this: DOI: 10.1039/c0xx00000x

www.rsc.org/xxxxxx

ARTICLE TYPE

TiO_2-Mesoporous Silica Nanocomposites: cooperative effect in the photocatalytic degradation of dyes and drugs

G. Zaccariello,[a] E. Moretti,[a]* L. Storaro,[a] P. Riello,[a,b] P. Canton,[a,b,c] V. Gombac,[d] T. Montini,[d] E. Rodríguez-Castellón[e] and A. Benedetti,[a,b,c]

Received (in XXX, XXX) Xth XXXXXXXXX 20XX, Accepted Xth XXXXXXXXX 20XX
DOI: 10.1039/b000000x

TiO_2-SiO_2 composites containing 10 wt.%, 20 wt.%, 30% and 40 wt.% of TiO_2, obtained by using preformed mesoporous silica nanoparticles MSNs and titanium isopropoxide as titanium source, have been investigated in detail using a variety of techniques. All the samples were characterized by N_2-physisorption, X-ray powder diffraction (XRPD), diffusive reflective UV–vis spectroscopy (DRUV-vis), X-ray photoelectron spectroscopy (XPS) and imaged using transmission electron microscopy (TEM). The TiO_2-MSN composites, that exhibited a spherical morphology, high specific surface areas and titania in the anatase phase, owing to their specific chemical-physical properties were studied as catalysts in the photocatalytic degradation of Methylene Blue, Methyl Orange and Paracetamol, as examples of polluted wastewaters. The well-defined porous structures of MSNs may offer a special environment for titania nanoparticles, increasing the specific surface area and the thermal stability of the composite, thus modifying the photocatalytic behavior of the materials. The TiO_2 loading, the particle size and the surface characteristics were related to the degree of UV absorption and the measured energy band gap of the nanocomposites. A cooperative effect between the two components (TiO_2 and SiO_2) could be the key factor at the basis of the good photocatalytic performances: nanostructured TiO_2 in intimate contact with MSN provides the sites for generation of $OH^{\bullet}$ radicals by oxidation of water and the SiO_2 skeleton is able to adsorb the molecules of cationic dyes and prevent poisoning of the TiO_2 surface.

Introduction

Titanium dioxide has been extensively studied as the most promising photocatalyst for the degradation of contaminants in solution because of its high photocatalytic activity, nontoxicity and low cost.

Titania is a heterogeneous semiconductor photocatalyst, which produces electron-hole pairs under ultraviolet light (200-400 nm) that initiates the formation of surface radicals capable of oxidizing adsorbed organic and biological pollutants. However, its exploitation has been restricted by a band gap energy (3.2 eV) that requires near UV wavelengths (387.5 nm) for efficient excitation and by the rapid recombination of charge carriers in the bulk. Generally the activity of anatase phase of TiO_2 in the photodegradation of organic, biological and pharmaceuticals pollutants is much higher than that of rutile.[1–3] Besides, it has been shown that the photocatalytic activity of TiO_2 can be influenced by crystal structure, surface area, crystallinity and porosity.[2] Many approaches have been used to obtain nano-sized titania samples in the anatase phase, such as chemical vapor synthesis,[3] the sol–gel method [4,5] and the hydrothermal [6–8] or solvothermal methods.[9] Moreover, the photocatalytic activity of anatase can be further improved by controlling the exposed surfaces, being the (001) the most active.[10,11]

The use of photosensitive semiconductors such as TiO_2 has been reported in the literature for its application in reducing colour of the dye solutions owing to its great advantages in the complete removal of organic pollutants from wastewater [12] and to the environmental-friendly benefits in the saving of resources such as water, energy, chemicals, and other cleaning materials.[4–7,13] However, one of the main drawbacks is the very poor adsorptive power to some organic pollutants.[14,15] It is well known that heterogeneous photocatalytic reactions mainly occur at the surface rather than in the solution bulk, and the surface properties of TiO_2 are critical for the efficiencies.[16,17] Many attempts have been made to modify the photocatalytic properties of titania.[18,19] TiO_2 were formed in specific structures and morphologies, with the aim to expose the most reactive faces instead of the most thermodynamically stable.[20–29] Band gap of TiO_2 can be reduced by doping with either metal [30–35] or non-metal elements.[35–40] On the other hand, in order to favour charge separation and/or extend the light absorption to the visible range, several kinds of TiO_2-based composites have been prepared using metal nanoparticles,[41–45] a second nanostructured semiconductor [46–53] or carbon nanostructures.[54–56] TiO_2 supported on microporous and mesoporous materials such as, alumina, silica, zeolites or clays were proposed as interesting materials taking advantage of the adsorptive properties of the second component.[14,15,27,57–61] The fabrication of mesoporous nanoarchitectures is of paramount

interest as quantum yield depends on crystal size and surface morphology, in addition high surface area and porosity promote the absorption and diffusion of the target molecules. In this last decade, silica nanoparticles with a controlled mesoporous structure (MSNs) have been extensively studied for the construction of variety of functional mesoporous nanomaterials.[62–67] Their properties such as well-defined and controllable morphology and porosity, chemical and thermal stability make them a highly suitable host matrix for incorporation of variety of active particles and molecules.

In this study we report the synthesis of TiO_2-SiO_2 composites containing 10 wt.%, 20 wt.%, 30% and 40 wt.% of TiO_2 obtained by the reaction of preformed mesoporous silica nanoparticles, MSNs, and titanium isopropoxide as titanium source. The resulting TiO_2-MSN composites, that exhibited a spherical morphology, high specific surface areas and titania in the anatase phase, owing to their specific chemical-physical properties, were studied as catalysts in the photocatalytic degradation of dyes (methylene blue and methyl orange) and drugs (paracetamol) in aqueous suspension.

Experimental

Materials

Tetraethoxysilane (TEOS, 98%), sodium hydroxide (NaOH), cetyltrimethylammonium bromide (CTABr), methanol (99.6%), titanium(IV) isopropoxide (TTIP, 97%), methylene blue (MB - 3,7-bis(Dimethylamino)phenazathionium chloride), methyl orange (MO - 4-[4-(Dimethylamino)phenylazo]benzenesulfonic acid sodium salt) and paracetamol were purchased from Sigma-Aldrich; n-hexane (99.6%) and ethanol (EtOH, 99.8%) from Carlo Erba. The water was distilled before use.

Synthesis of mesoporous silica nanoparticles (MSN)

For the synthesis of mesoporous silica nanoparticles, the procedure described by Ma et al. was adopted.[68] An initial solution was prepared mixing CTABr (0.2 g), NaOH 2 mol/L (0.75 mL) and H_2O (100 mL) under stirring. Once the solution was clear, n-hexane (15 mL) were added and then stirred for 15 min (400 r/min). The stirring was stopped to allow the separation between the polar and non polar phases and TEOS (1 mL) was dropped slowly into the solution. The system was immediately put under vigorous stirring and the obtained solution was kept under stirring, at room temperature, for 5 h. The molar ratio of the reagents used for the synthesis was 1 TEOS: 0.12 CTABr: 1268 H_2O: 0.32 NaOH: 2.7 n-hexane. The system was filtered and the recovered solid product was washed several times with methanol and dried at 60°C overnight. A calcination at 550°C for 5h (with a heating rate of 2°C/min) was performed in order to remove the surfactant (CTABr) from the material. The obtained sample was referred as MSN.

Synthesis of the TiO_2 nanoparticles loaded into MSN matrix ($xTiO_2$-MSN)

TiO_2 nanoparticles were loaded into calcined silica MSN at room temperature by incipient wetness impregnation. The nanocomposites were synthesized with different TiO_2 loadings and they were referred as $xTiO_2$-MSN, where x represents the weight percentage of TiO_2 calculated in the total nanocomposite. The procedure of incorporating TiO_2 into the pores of MSN is that reported by Lihitkar et al.[69] with slight modifications. In our typical synthetic procedure, the reaction was carried out under nitrogen flow. Different amounts of titanium tetraisopropoxide were dissolved in EtOH (25 ml) and each mixture was added to calcined silica (0.2 g) under magnetic stirring for 24 h. Then, the solvent was evaporated and the recovered solids were calcined at 550°C, 2°C/min rate, for 5 h.

Characterization

TGA-DTG thermogravimetric analyses were performed in air from 30°C to 900°C with a heating rate of 20°C/min with a thermobalance Netzsch STA 409.

Adsorption-desorption isotherms of nitrogen were obtained at the liquid nitrogen temperature using a Micromeritics ASAP 2010 system. Each sample has been degassed at 130 °C overnight before measuring the N_2 physisorption isotherm. From the data, the Brunauer-Emmett-Teller (BET) equation and the Barrett-Joyner-Halenda (BJH) model were used to calculate the specific surface area and the pore size distribution, respectively.

X-ray powder diffraction (XRPD) analyses were recorded with a Philips X'Pert powder diffractometer (Bragg-Brentano parafocusing geometry). A nickel-filtered Cu Kα1 radiation (λ = 0.15406 nm) and a voltage of 40kV were employed.

Size and morphology of the nanoparticles were studied through a JEOL JEM 3010 transmission electron microscope (TEM) operating at 300 kV; the powder specimens were suspended in isopropyl alcohol and then sonicated, 5µl of this suspension were deposited on a copper grid (300 mesh) coated with holey carbon film. The copper grids were allowed to dry in air.

The diffusive reflective UV–vis (DRUV-vis) spectra were collected with a JASCO V-570 UV-vis spectrophotometer. The powder samples were loaded in a quartz cuvette and the spectra were recorded in 200-800 nm wavelength range. The absorption coefficient (α) can be calculated from the following formula: $\alpha = ln(1/T)/d$, where T is the measured transmittance and d is the optical path length. Band gap energy, E_g, was determined thoroughly the absorption coefficient α (m^{-1}) from a plot of $(\alpha h\nu)^2$ versus photon energy ($h\nu$), where h is Planck's constant (4.135×10^{-15} eV·s) and ν is the frequency (s^{-1}). The intercept of the tangent to the absorption curves was used to estimate the band gap energy.

X-ray photoelectron spectra (XPS) were collected using a Physical Electronics PHI 5700 spectrometer with non monochromatic Mg Kα radiation (300W, 15 kV, 1253.6 eV) for the analysis of the core level signals of C 1*s*, O 1*s*, Ti 2*p* and Si 2*p* and with a multi-channel detector. The spectrometer was calibrated using the signal Au $4f_{7/2}$ = 83.9 eV. Binding energy values were referenced to the C 1*s* peak (284.8 eV) from the adventitious contamination layer. The *PHI ACCESS ESCA-V6.0 F* software package and *Multipak v8.2b* were used for acquisition and data analysis, respectively. A Shirley-type background was subtracted from the signals. Recorded spectra were always fitted using Gauss-Lorentz curves, in order to determine the binding energy of the different element core levels more accurately. The error in BE (binding energy) was estimated to be *ca.* 0.1 eV.

Photocatalytic Degradation

The degradation of two representative dyes (methylene blue – MB – and methyl orange – MO) and of paracetamol were chosen as test reactions to evaluate the photocatalytic activity of the synthesized materials under UV-vis irradiation. A 100 ml Pyrex photochemical reactor with a 125W medium pressure mercury lamp (model UV13F, Helios Italquartz, Italy) was used. The initial concentrations of target molecules were $6.0x10^{-5}$ M for MB, $7.5x10^{-5}$ M for MO and $1.3x10^{-4}$ M for paracetamol. The amount of the photocatalyst was fixed at 1.25 g/L. All the degradation experiments were carried out at 293 K. The photon flux was measured by using a DeltaOHM radiometer HD2302.0 leaned against the external wall of the photoreactor containing only pure water. The irradiation power was 29mW/cm^2 in the UV-A range (310 - 400 nm) and 100 mW/cm^2 in the visible/near IR range (400 - 1050 nm). To reach the adsorption equilibrium before irradiation, the suspension was stirred in the dark for 30 min.[70] After switching on the lamp, aliquots of 2 ml of the aqueous suspension were collected from the reactor and filtered through a 0.45 µm PTFE Millipore disc to remove the catalyst powder.

A Shimadzu Uv-2450 UV/Vis spectrometer was used for the determination of the dye concentration, after calibration. The degradation processes were monitored following the absorbance at the maximum of the UV-vis spectrum of the target molecules (660 nm for MB, 465 nm for MO and 243 nm for paracetamol). Since the degradation pathways for the selected dye are known with high reliability,[71–75] the eventual formation of by-products was checked monitoring the overall UV-vis spectrum of the solutions recovered at different times during the degradation experiments. The mineralization of the target molecules and the production of intermediate inorganic species have been checked by ionic chromatography, using a Metrohm 883 instrument equipped with a conductometric detector. The inorganic anions were analyzed using a Metrosep A Supp5 250/4.0 column using a $NaHCO_3$ 1mM / Na_2CO_3 3.2 mM solution as mobile phase while the cations were analysed using a Metrosep C4 250/4.0with HNO_3 4.0mM as mobile phase.

For each target molecule, the material that demonstrated the best photocatalytic performance has been chosen to assess the reusability of the present nanocomposites. After switching off the lamp at the end of the first degradation experiment, a certain amount of the target molecule and of the photocatalyst was added into the reactor of the photocatalyst in order to restore the initial concentrations. After equilibration in the dark for 30 min, the lamp was switched on and samples of the solution (2 mL) were collected during time for UV-vis analysis. Four cycles have been performed for each target molecule.

Results and discussion

Thermogravimetric analysis

TGA analysis was performed from 25 to 1000°C under air flow, in order to determine the post-synthesis thermal treatment to be applied to the bare siliceous matrix MSNs, to completely remove the organic phases of the surfactant and of the silica precursor. From Fig.1, it is evident that the majority of weight loss occurs at temperatures lower than 400°C. An initial weight

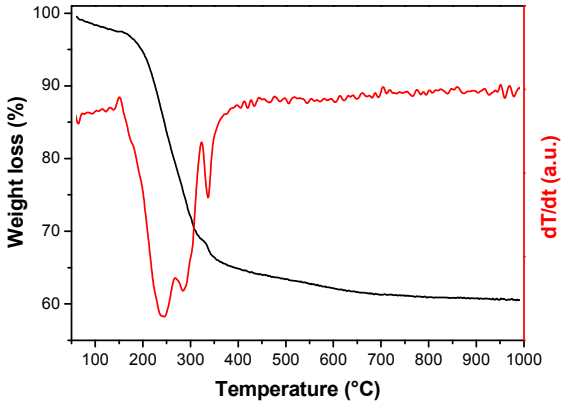

Fig. 1 Thermogravimetric curve of bare mesoporous silica nanoparticles MSN. The dotted curve is the first derivative of the weight loss (DTG).

loss of 5% is due to the removal of residual solvent. A second minimum at 250°C, visible in the derivative of thermogravimetric curve (DTG), has been ascribed to the removal of the organic fraction comprising CTABr which has a melting point of 237°C and decomposes at around 243°C. The slight difference with the reported values could be due to its encapsulation in the pores, which creates an interaction between the surfactant molecules and the internal surface of the MSNs. In the 250-550°C temperature range the combustion of unreacted ethoxy groups arising from TEOS, the decomposition of residual organic molecules and the condensation of neighbouring silanol groups occurred. Above 550°C a further loss of approximately 2% was observed due to thermal dehydroxylation of internal surface silanol groups to form siloxane bridges. After this preliminary study, the MSNs support was calcined at 550°C.

N_2 Physisorption

Fig. 2a shows the N_2 adsorption-desorption isotherms at the liquid nitrogen temperature of the calcined mesoporous silica compared to the xTiO_2-MSN composites containing different amounts of titania. The textural parameters (specific surface area, pore size distribution and specific pore volume) are reported in Tab. 1.

The isotherm of the calcined silica MSN displays the type IV profile with a H1 hysteresis loop (according to the IUPAC classification),[76] typical of ordered and mesoporous materials with one-dimensional cylindrical channels. The bare silica shows a high BET specific surface area (900 m^2/g) and the distribution of the pore diameter, according to the BJH model applied on the adsorption branch, is very narrow and centred at 4.3 nm (Tab.1).

After the impregnation with different TiO_2 loading, all the xTiO_2-MSN composites maintain a type IV isotherm profile. This means that the very ordered mesoporous channels of the silica matrix are kept intact after the formation of TiO_2 nanoparticles (Fig. 2b).

Furthermore, the loading of titania nanoparticles gives rise to a decrease of the amount of adsorbed nitrogen. The capillary condensation that causes the filling of the mesopores occurs at relative pressures p/p_0 in the range of 0.4-0.6. Furthermore, the size and the distribution of the pores characterize the inflection points and the sharpness of the isotherms.[77]

Table 1 Physicochemical parameters derived from nitrogen physisorption of the MSN and $xTiO_2$-MSN samples and from XRD measurements of TiO_2 crystallite size.

Sample	[a]$S.A._{BET}$ (m^2/g)	[b]D_p (nm)	[c]V_p (cm^3/g)	[d]D_c (nm)
MSN	900	4.3	0.90	-
$10TiO_2$-MSN	720	4.3	0.84	2.8
$20TiO_2$-MSN	665	4.2	0.76	2.6
$30TiO_2$-MSN	505	4.3	0.69	6.8
$40TiO_2$-MSN	411	4.3	0.57	13.7

[a] BET specific surface area ($S.A._{BET}$);

[b] Mean pore size (D_p);

[c] Total pore volume (V_p);

[d] TiO_2 XRD average crystallite size (D_c). The estimated error is ±10%.

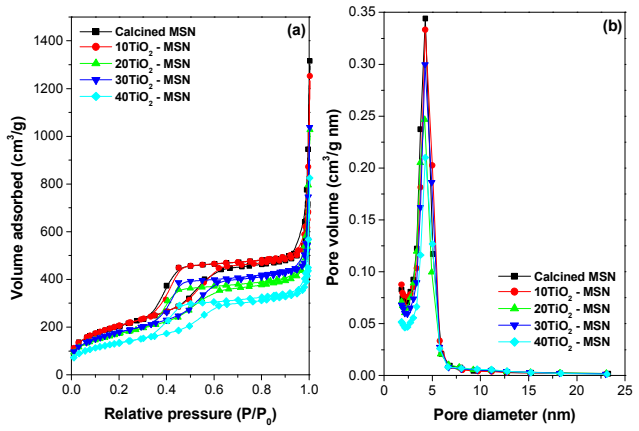

Fig. 2 (a) N_2 adsorption-desorption isotherms of the bare silica nanoparticles and the $xTiO_2$-MSN nanocomposite materials; (b) BJH pore size distribution estimated on the adsorption branch of the calcined samples.

A comparison of the textural properties of the $xTiO_2$-MSN nanocomposites with that of the bare silica matrix indicates that, while the maximum of the pore size distribution is almost constant for all the samples, the specific surface area and the total pore volume of the TiO_2-MSN samples decrease with the increase of TiO_2 loading. This suggests that titania should be confined inside the pores of the silica matrix or blocking the channels aperture, causing the partial filling of the pores of pristine MSN.

X-Ray Powder Diffraction

The XRPD profile of the calcined MSN silica (not shown) exhibits two well-resolved diffraction peaks, at $2\theta = 1.60 \pm 0.05°$, $2.60 \pm 0.05°$ indexed as (100), (110), associated to an ordered hexagonal mesoporous materials. The lattice constant (a_0) and the pore wall thickness (w_p) of the bare nanostructured silica are: 6.6±0.3 nm and 2.3±0.4 nm respectively. As the material is not crystalline at the atomic level, no reflections at higher angles were observed. Fig. 3 displays the XRPD patterns of the four nanocomposite samples.

In the low angle region (inset of Fig. 3), the $xTiO_2$-MSN composites show XRD profiles similar to that of the MSNs support, indicating that the hexagonal ordered structure of silica

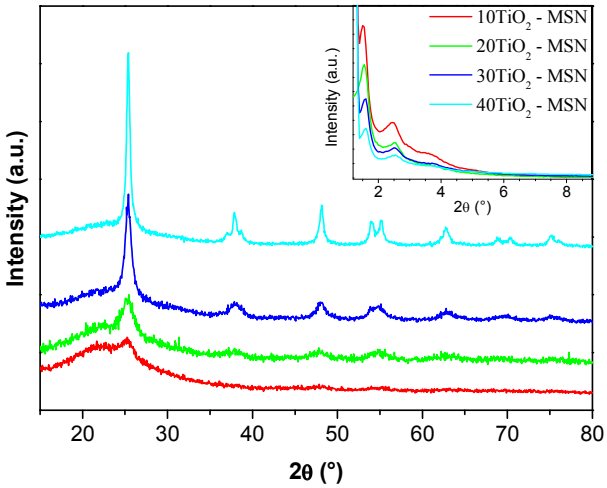

Fig. 3 XRPD patterns of the four $xTiO_2$-MSN samples in the wide-angle region. In the inset the low-angle region is reported.

matrix is well retained and the loading of TiO_2 into the pores of the MSN does not cause a collapse or a modification of the silica network and its morphology.

As expected, a decrease of intensity is observed in these reflections and it can be ascribed to the filling of the silica pores that cause a reduction of the scattering contrast between the channels and the pore walls of the silica.[77] Nevertheless, the pattern is conserved confirming that the hexagonal arrangement of ordered mesoporous MSNs is retained even after the incorporation of titania nanoparticles into the channels of the silica matrix.

In the XRD wide-angle region, the patterns of all the $xTiO_2$-MSN samples calcined at 550°C exhibit reflections at 2θ values corresponding to the characteristic pattern of anatase (the only present crystalline phase of TiO_2, PDF 21-1272).

The crystallite sizes of titania in the $xTiO_2$-MSN samples were determined by Line Profile Analysis (LPA)[78] of the peaks corrected for the instrumental broadening. The crystal sizes of the samples based on the volumetric average are reported in Tab.1.

Transmission Electron Microscopy

TEM micrograph of the bare silica (Fig.S1a) shows an ordered two-dimensional hexagonal mesoporous structure with pore diameter of about 5 nm, in agreement with the BJH distribution. The silica nanoparticles have spherical morphology, with diameter ranging from 100 to 200 nm.

TEM micrographs of the specimens containing TiO_2 (Fig. S1b, c, d, e) are reported, showing the crystal lattice fringes of titania nanoparticles.

The size distribution of TiO_2 is somewhat heterogeneous (from 1.8 to 5.0 nm) but in agreement with the silica pores size. These results are coherent with the average crystallite size obtained by LPA. For the $10TiO_2$-MSN specimen the main size distribution of titania nanoparticles is in the range between 2 and 3 nm; whereas for $20TiO_2$-MSN it is around 3-4 nm (Fig. S1b, c). Fig. 4 reports low magnification micrographs for all the TiO_2-containing specimens. $10TiO_2$-MSN and $20TiO_2$-MSN materials show no TiO_2 particles on the MSN surface. The $30TiO_2$-MSN specimen shows a small fraction of the titania nanoparticles decorating the

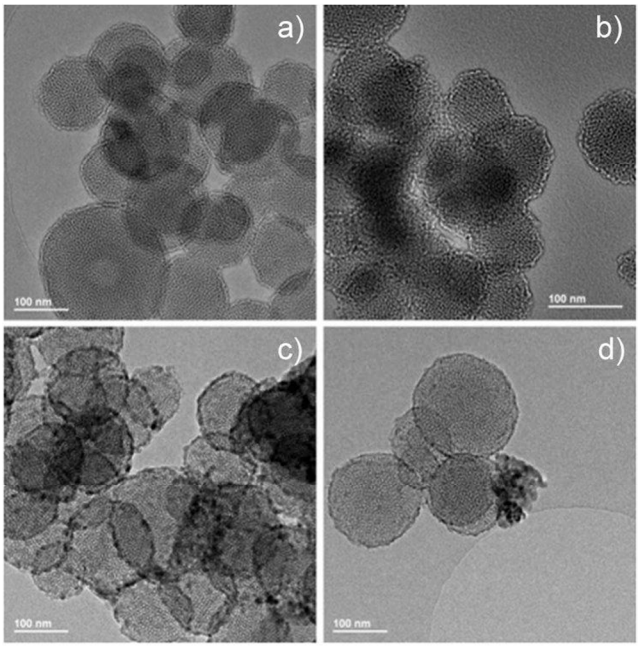

Fig. 4 Representative TEM micrographs of (a) $10TiO_2$-MSN, (b) $20TiO_2$-MSN, (c) $30TiO_2$-MSN and (d) $40TiO_2$-MSN.

surface of silica and an average crystallite size slightly larger than the size of the silica pores. TEM picture (Fig. 4d) of $40TiO_2$-MSN reveals a decoration of TiO2 nanoparticles on the surface of MSN and also a consistent growth of larger TiO_2 nanoparticles outside the MSN with sizes ranging from 7.5 to 12 nm.

From these experimental observations, it could be inferred that, in case of lower content of TiO_2 ($10TiO_2$-MSN and $20TiO_2$-MSN materials), the channels of the silica are able to control the growth of titania nanoparticles keeping their sizes within the silica pore diameters (i.e. lower than 5 nm). In the case of higher TiO_2 contents ($30TiO_2$-MSN and $40TiO_2$-MSN specimens), TEM micrographs evidence the existence of two different size distributions of nanoparticles: one distribution having an average size below the average diameter of the silica pore, while the second size distribution is characterized by particle sizes much bigger. These observations could suggest that there is a threshold concentration below which the titania is able to grow inside the channels of SiO_2; when this threshold is exceeded, the growth of TiO_2 takes place also on the external surface of the silica network, forming large aggregates as the TiO_2 content increases.

The Selected Area Electron Diffraction (SAED) performed in the $xTiO_2$-MSN specimens provides a series of ring patterns that can be indexed as the anatase phase of TiO_2, in agreement with the results obtained by XRD.

The EDX measurements carried out inside the MSN show the presence of the chemical element Ti, Si and O.

XPS

The surface chemical analysis of the composite samples has been carried out by XPS. The binding energy value for Ti $2p_{3/2}$ shifts to lower values with the content of titania and presents a value of 458.3 eV for sample $40TiO_2$-MSN. This value is very similar to that reported for pure TiO_2 nanospheres.[79] The binding energy values of Si 2*p* (103.3-103.5 ev) are typical to that found for SiO_2. The relative intensities of Si and Ti signals show that the

Table 2 Comparison between the theoretical and surface (determined by XPS) Si/Ti atomic ratios and band gap energies for the studied $xTiO_2$-MSN nanocomposites.

Sample	Si/Ti theoretical	Si/Ti surface	Energy gap (eV)
$10TiO_2$-MSN	11.96	4.11	3.26
$20TiO_2$-MSN	5.32	3.34	3.26
$30TiO_2$-MSN	3.10	1.77	3.22
$40TiO_2$-MSN	2.00	1.24	3.20

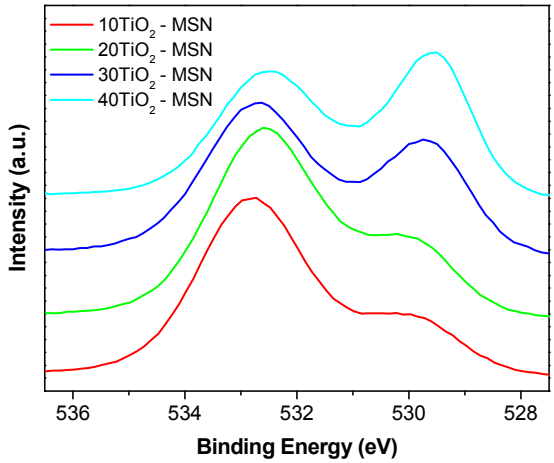

Fig. 5 O1s core level spectra for samples $10TiO_2$-MSN, $20TiO_2$-MSN, $30TiO_2$-MSN and $40TiO_2$-MSN.

values of surface Si/Ti atomic ratios are always lower than the theoretical ones. This is indicative that titanium is mainly on the surface of the solid. With higher contents of titanium the observed difference is less pronounced. That is, in the case of samples $40TiO_2$-MSN the surface Si/Ti ratio is 1.24 and the theoretical one is 2.00. This suggests that, with a high content of titanium, the fraction of titanium incorporated into the mesoporous channels is much higher.

The evolution of the O 1s core level signals with the content of TiO_2 is presented in Fig. 5. These spectra can be decomposed in at least three contributions at 530.1, 531.1 and 532.8 eV (Fig. SX shows, as an example, the deconvolution obtained for the $10TiO_2$-MSN material). The contribution at higher BE is assigned to oxygen from SiO_2 while the one at lower BE is attributed to oxygen from TiO_2.[80] The contribution at 531.1 eV has been attributed to Ti-O-Si.[81] The O 1s spectra presented in Fig. 5 suggest that significant differences are present in the materials depending on the TiO_2 content. The relative intensity of the contribution at 531.1 eV is appreciable for samples $10TiO_2$-MSN and $20TiO_2$-MSN, where a strong interaction between titania and silica occurs. This is in agreement with the formation of small anatase crystallites (as evidenced by XRD), in strong contact with SiO_2 mainly within the channels of MSN. The contribution at 531.1 eV is very weak while the relative intensity of the contributions due to titania at 530.1 eV shows a significant increase for the samples with higher titania contents, in agreement with the formation of TiO_2 nanoparticles on the external surface of MSN. These results, in combination with TEM analysis of the materials, suggest that a critical threshold in the TiO_2 loading exists between 20 and 30 wt%. Below this threshold, a strong interaction between SiO_2 and TiO_2 takes

place, resulting in highly dispersed Ti-species and/or small TiO_2 nanoparticles mainly inside the MSN channels. Above the critical threshold, the amount of TiO_2 is large enough to completely cover the surface and the growth of TiO_2 nanoparticles takes place also on the external surface of the MSN, as revealed by TEM and XPS. Moreover, the mean crystallite size of TiO_2 increases because their growth is not limited by the nanometric diameter of the pores of MSN.

UV-vis

The diffuse reflectance UV-vis spectra $xTiO_2$-MSN samples are presented in Fig. 6, evidencing that a strong absorption of light takes place on these materials below 400 nm. As a comparison, the diffuse reflectance UV-vis of the pristine MSN is presented in Fig. S2, demonstrating that the contribution of MSN is negligible in this range.

As it is clearly evident, the decrease of titania content corresponds to a shift of the UV absorption edge to shorter wavelengths. Plots of $(\alpha h\nu)^2$ versus photon energy $(h\nu)$ are shown in the inset of Fig. 6. The same methodology have been previously adopted to determine the band gap of TiO_2-SiO_2 composite materials.[82,83] The energy band gap values were found to be in the range of 3.20 – 3.26 eV. In particular, the E_g decrease with the increase of titania content (Table 2). The blue shift in the absorption edges and the correspondent increase in the bang gap values could be reasonably associated to the well-known quantum size confinement resulting from the decrease in crystallite size by the.[77,84,85] This effect has been previously observed in the case of other TiO_2-SiO_2 composites prepared by different techniques.[86–90] The origin of the blue shift in the absorption edge has been ascribed to the existence of Ti–O–Si chemical bonds.[89,90] In agreement with this, in the present $xTiO_2$-MSN composites, the largest blue shift is observed for the materials with the lower TiO_2 content, in which the Ti-O-Si contribution represents the most important Ti-related species as revealed by XPS.

Photocatalytic activity

The $xTiO_2$-MSN composites were studied as catalysts in the photocatalytic degradation of dyes (methylene blue and methyl orange) and drugs (paracetamol) in aqueous suspension.

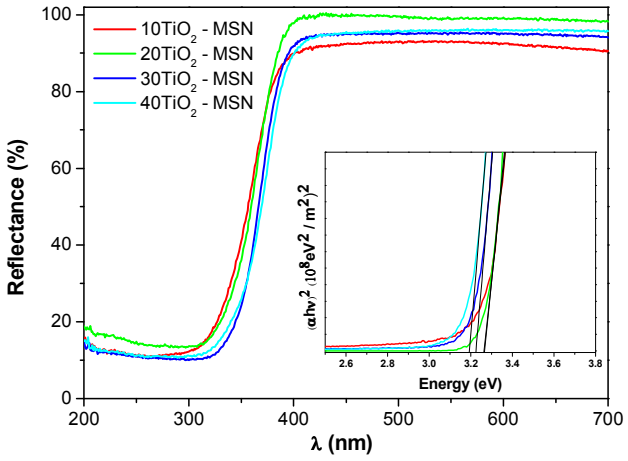

Fig. 6 Diffuse reflectance UV-Vis spectra of the TiO_2-MSN composites and the $(\alpha h\nu)^2$ against photo energy $(h\nu)$ of the TiO_2-MSN composites (inset).

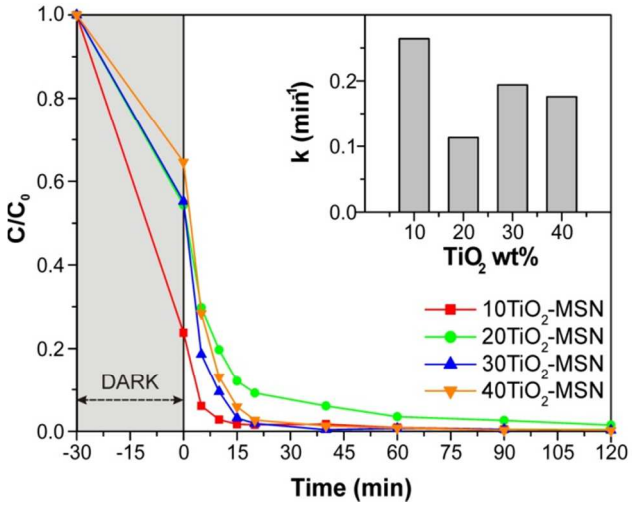

Fig. 7 Performances of adsorption and MB photodegradation on $xTiO_2$-MSN catalysts before and under UV-vis irradiation, with the calculated kinetic constants (inset).

Methylene blue (MB) degradation

Fig. 7 presents the decrease of MB concentration as a function of time during photocatalytic experiments in the presence of the TiO_2-MSN materials under UV-vis irradiation.

After 30 min of equilibration in the dark, a high amount of MB is adsorbed on the surface of the materials, decreasing from 75% to 35% as the fraction as the TiO_2 amount increases from 10 wt% to 40 wt%. This could be related to the decrease in surface area observed increasing the content of TiO_2 and with a potential selective adsorption of MB on the SiO_2 fraction of the TiO_2-MSN materials. Notably, the pristine MSN support adsorbs ~ 50% of the dye (not shown). In the case of a charged dye, the quantities adsorbed in the dark depend on both the surface area and the Point of Zero Charge (PZC) of the materials. In the case of the TiO_2-SiO_2 composites, PZC values usually lower than 4 pH unit were reported.[91,92] Therefore, in our working conditions (slightly acidic pH), the surface of the catalysts is deprotonated and covered by negatively charged moieties, able to adsorb large quantities of the cationic dye MB, especially on the SiO_2 exposed surface. The adsorption of large amounts of cationic dyes on SiO_2-TiO_2 materials was in fact reported in the literature.[91,92]

After switching on the UV-vis lamp, the concentration of MB decreases exponentially with the time for all the $xTiO_2$-MSN samples. Pseudo-first order kinetic constants are calculated plotting $\ln(C_0/C)$ vs time for the first part of the exponential decay curves. The values of the kinetic constants k are reported in the inset of Figure 7. The highest value of k (0.264 min^{-1}) is obtained for $10TiO_2$-MSN, although this result could be influenced by the very high MB adsorption observed for this material (75%). On the other hand, the other samples investigated, that show comparable MB adsorption properties (35–45%), present a trend in the values of k with a relative maximum for $30TiO_2$-MSN (0.194 min^{-1}).

The pathway for MB degradation on TiO_2-based materials has been studied in detail by Houas et al. by LC/MS and GC/MS

analysis of the intermediate compounds.[72] The degradation of MB starts with the oxidation of S to form a sulphonic group and the opening on the central aromatic ring and the formation of an NH_2 group. Further oxidation by reaction with $OH^{\bullet}$ leads to the dissociation of the two benzenic rings, with the formation of sulphonic acid and aniline substituted with dimehtylamino groups. Subsequent reaction of these intermediates with $OH^{\bullet}$ leads to the formation of hydroxylated phenols, the opening of the aromatic ring and its mineralization through the formation of carboxylic acids. The degradation of the aromatic ring is accompanied by the release of sulphates and ammonium ions into the aqueous media. To check the presence of intermediates in solution, UV-vis spectra in the 300 – 900 nm range of the solutions were collected at different reaction time (Figure S3): no new absorption bands, indicating that the organic by-products are easily oxidized and decomposed to small fragments. The IC analysis of the solutions recovered at the end of the degradation experiments showed the presence of chlorides and sulphates in good stoichiometric ratio with respect to the initial MB concentration. Moreover, traces of anions such as formiate, acetate, oxalate and nitrate, and of cations such as ammonium ions have been detected. Formiates, acetates and oxalates are intermediate products of the degradation of the organic skeleton. Ammonium ions are released from the N-containing functional groups of the MB molecules and are partially converted into nitrates during photocatalytic degradation.[93,94] These results suggest that skeleton of MB is completely destroyed during the photocatalytic experiments leaving inorganic ions and only minor amounts of non-toxic compounds.

The 30TiO2-MSN material, that demonstrated the best photocatalytic performances, was chosen for the reusability test. After the first degradation experiment, MB was introduced in the reactor restoring the initial concentration. The degradation of the dye was monitored during 4 consecutive cycles (Figure S4), observing a slight minimal decrease in the photocatalytic performances of the material. Nevertheless, complete removal of MB is always achieved after 2h of irradiation. The progressive deactivation observed could be related with the progressive accumulation in the solution of inorganic anions, such as chloride, sulphates and nitrates.

The results from photocatalytic degradation of MB over the $xTiO_2$-MSN samples suggest that a strong synergy between the two components of the materials (TiO_2 and SiO_2) are required to obtain the best performances in water remediation. The role of the two components (TiO_2 and SiO_2) is complementary: SiO_2 adsorbs the cationic dye from solution through electrostatic attraction of the surface $Si\text{-}O^{\delta-}$ groups, while the anatase TiO_2 nanocrystals provide the photoactive sites producing the $OH^{\bullet}$ radicals required for the MB degradation. In this context, the maximum in activity demonstrated by $30TiO_2$-MSN could be rationalized considering that this composition is just above the critical threshold of the TiO_2 incorporation inside the channels of MSN, presenting TiO_2 nanoparticles mainly located inside the pores with a small fraction decorating the surface of MSN. This finding results in the closest interaction between the sites of adsorption of MB and the sites for $OH^{\bullet}$ production inside the mesopores of MSN. Similarly, a cooperative effect between TiO_2 and SiO_2 was previously reported in the degradation of cationic dyes [91,92] for materials with higher TiO_2 contents (60-90%). In these studies, the authors suggested that inner surface of pores was pre-enriched by adsorption of the dye in SiO_2 surface. The degradation of the dye was promoted by the photoactive TiO_2 moieties while the complete mineralization was possible due to the confinement of intermediate products inside the mesopores. Beyers et al. [95] demonstrated that the inclusion of TiO_2 nanoparticles (both for anatase and rutile phases) inside the pores of SiO_2-based materials is essential to obtain a high photocatalytic activity in the degradation of cationic dyes.

Methyl Orange (MO) degradation

The $xTiO_2$-MSN materials were also tested in the photocatalytic degradation of methyl orange, which is negatively charged in a wide pH value range.

Figure 8 shows the decrease of MO concentration with time during photocatalytic experiments using the four $xTiO_2$-MSN catalysts. The amount of MO adsorbed on the materials in the dark, measured at the time t = 0, is proportional to the amount of TiO_2 present in the composite, increasing from 1.8% to 21.8% of the initial amount of MO moving from $10TiO_2$-MSN to $40TiO_2$-MSN. This result suggests that, differently from the case of MB, MO adsorption could take place preferentially on the TiO_2 nanoparticles. The PZC of anatase is reported to be 5.3 – 5.6, depending on the preparation condition and measurement technique,[96] values close to the natural pH of the dye solution (slightly acidic pH). Therefore, the adsorption of an anionic dye, such as MO, is less favored with respect to a cationic dye (MB) and, in any case, should take place on the TiO_2 phase, presenting a PZC value significantly higher than that of the SiO_2 part.

The photocatalytic activity in the decolourization of MO increased up to the TiO_2 content of 30wt%, while a further increase to 40wt% resulted in a significant decrease of the performance. In agreement with this, the kinetic constants, calculated on the basis of a first-order kinetic, show a maximum for the $30TiO_2$-MSN material (0.0699 min^{-1}).

The pathway of photocatalytic degradation of MO in aqueous solution has been studied by HPLC-MS by Baiocchi et al.[71] The reaction of MO with photo-generated $OH^{\bullet}$ results, in different order, to the hydroxylation of the aromatic rings, demethylation of the dimethylamino group and substitution of the sulphonic

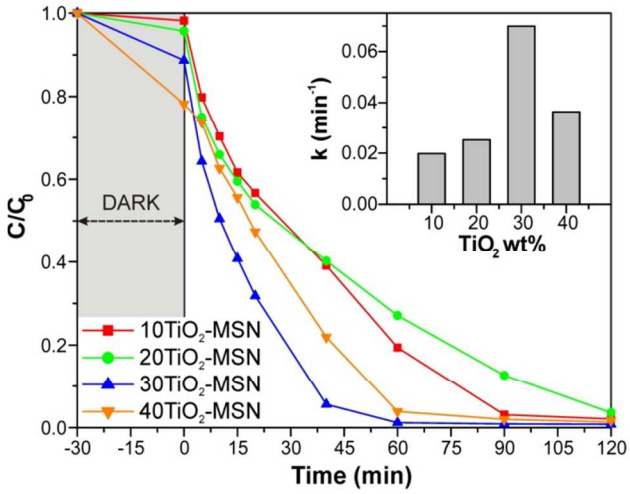

Fig. 8 Performances of adsorption and MO photodegradation on $xTiO_2$-MSN catalysts before and under UV-vis irradiation, with the calculated kinetic constants (inset).

group with a OH group. Further oxidation and fragmentation of the molecule leads to the aniline and sulphonic acid, eventually hydroxylated on the aromatic ring and/or substituted with the azo group. Finally, further degradation produces sulphates, N_2 and NH_4^+ and different carboxylic acids after oxidation and opening of the benzenic ring. The presence of organic by-products has been checked analyzing the UV-vis spectra in the 300 – 900 nm range of the solutions collected at different reaction times. Also in this case, the appearance of new absorption bands was not observed (Figure S5), indicating that degradation of MO and of its aromatic by-products were fast under the photocatalytic conditions adopted.

The IC analysis of the solutions recovered at the end of the degradation experiments showed the presence of Na^+ in good stoichiometric ratio with respect to the initial MO concentration and traces of NH_4^+ deriving from the degradation of dimethylamino group. Also in this case, traces of anions such as formiate, acetate, oxalate, sulfates and nitrate have been detected, as intermediate products of the degradation of the organic skeleton and from the oxidation of NH_4^+.[93,94] Notably, the amount of $SO_4^=$ ions detected in solution is in good stoichiometric ratio with the initial amount of MO. These results indicate that skeleton of MO is completely degraded during the photocatalytic experiments with the production of inorganic ions and only minor amounts of non-toxic compounds.

The trend observed for MO decolourization on $xTiO_2$-MSN nanocomposites (Figure 8) could be due to the combination of various factors. The adsorption of MO takes place mainly on the TiO_2 surface, with various important consequences:

i) the surface of TiO_2 nanoparticles is less available for the adsorption of water, reducing the possibility to produce $OH^\bullet$ radicals responsible for the dye degradation in solution;

ii) considering the absorption spectrum of the dye, MO (both adsorbed and/or in solution) could act as a light filter, reducing the number of photons with the correct energy approaching the surface of the photocatalyst and therefore reducing the ability to produce the radical species responsible for dye decolourization;

iii) at the same time, adsorbed MO could act as a sensitizer, absorbing photons and transferring electrons from the excited state of the dye to the conduction band of TiO_2.[97]

The first two possibilities suppress the photocatalytic activity while the latter enhances the performances of the semiconductor photocatalysts. In the present case, the $30TiO_2$-MSN material shows the best photocatalytic performances as a result of the best compromise between the opposite effects induced by adsorbed MO. For this reason, the $30TiO_2$-MSN nanocomposite has been selected for the reusability test, obtaining the results presented in Figure S6. The performance of the present photocatalyst slightly decreases during various cycles of reaction, although the complete decolourization of MO solution is always achieved within the 2h of irradiation. Also in this case, this result can be related with the accumulation of the inorganic by-products (Na^+, NH_4^+, sulphates, nitrates) in the aqueous solution, ions that can be adsorbed on the surface of the TiO_2 and/or SiO_2 components affecting all the processes taking place on the surface of the material (adsorption of the target molecule and possible by-products and production of $OH^\bullet$ radicals by photo-oxidation of water or photo-reduction of dissolved O_2).

Paracetamol degradation

Finally, the $xTiO_2$-MSN materials were tested in the photocatalytic degradation of paracetamol, as a model reaction for the purification of water from pollutant drugs. Moreover, paracetamol is a neutral molecule and contains a phenolic ring, one of the most recalcitrant moiety to be degraded by decontamination techniques. The degradation of paracetamol as a function of irradiation time under UV-vis light is presented in Fig. 9.

As to paracetamol, the amount adsorbed on the surface of the photocatalysts is always negligible (lower than 2%), because of the neutrality of the target molecule.

During irradiation with UV-vis lamp, the behavior of the $xTiO_2$-MSN photocatalysts depends on the amount of TiO_2. In the case of $10TiO_2$-MSN and $20TiO_2$-MSN, the concentration of paracetamol decreases monotonically. At the same time, the appearance of new bands is observed in the UV-vis spectra of the solution samples recovered during the photocatalytic experiments (Figure S7). These new bands are centered at 215 nm, that is present also after complete conversion of paracetamol, and at 320 nm, even with a low intensity and disappearing after 30 – 40 min of irradiation. On the other hand, increasing the amount of TiO_2 present in the composite materials, the degradation of paracetamol is very fast in the initial 20 minutes. After this period, the concentration of paracetamol decreases slowly and, after 90 minutes of irradiation, the degradation rate increases again. In these last cases, the band at 215 nm is always less intense than that observed in the case of the materials with a lower loading of TiO_2 and the intensity of the band at 320 nm is always negligible (Figure S7).

The mechanism of paracetamol degradation under photocatalytic conditions (mainly under UV-vis irradiation) have been previously reported in the literature.[73,74] Generally, the reaction involves, in a different order, the deacylation of the

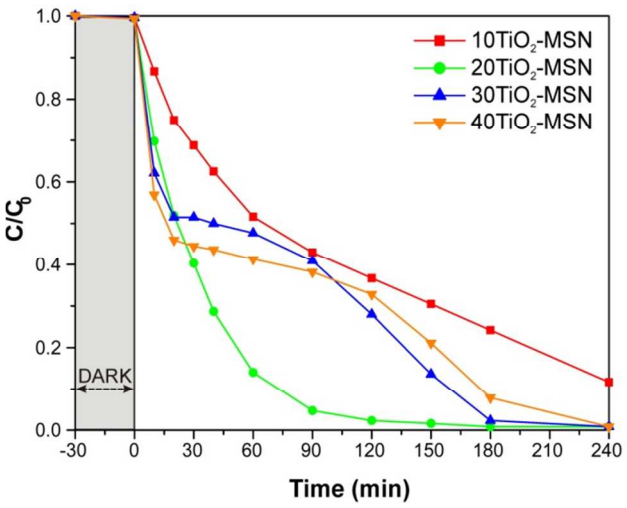

Fig. 9 Degradation profile of paracetamol solution using the various $xTiO_2$-MSN catalysts under UV-vis irradiation.

molecule and the hydroxylation of the aromatic ring, producing *p*-aminophenol, N-(3,4-dihydroxyphenyl)-acetamide, N-(2,4-dihydroxyphenyl)-acetamide and hydroquinone as intermediates. Finally, the phenolic ring is broken by reaction with $OH^{\bullet}$ radicals, producing dicarboxylic acids, that will be further degraded until complete mineralization. The formation of *p*-aminophenol has been evidenced by the increase in the absorbance at 320 nm [73] while absorption band around 215 nm can be associated with the formation of the dicarboxylic acids. Moreover, the IC analysis of the solutions recovered at the end of the degradation experiments revealed the presence of NH_4^+, NO_3^-, formiates, acetates and oxalates. NH_4^+ is the product of the mineralization of the amide group of paracetamol and produces nitrates by oxidation [93,94] while the other by-products represent the last steps in the degradation of the dicarboxylic acids produced by the opening of the phenolic ring.

The studied xTiO_2-MSN composites show a very different behavior depending on the loading of TiO_2. This is the result of the different morphology of the materials observed by TEM as the amount of TiO_2 increases. Anatase nanoparticles are located mainly inside the mesopores of the MSN materials up to a loading of 20 wt% and molecules in the solution must diffuse inside the mesopores to reach the photocatalytic sites. Considering the small dimension of the pores of the TiO_2-MSN materials (~ 4.3nm), the diffusion of paracetamol could be strongly hindered with respect the diffusion of water. Moreover, paracetamol is only weakly adsorbed on the surface of the composite materials. Therefore, it is reasonable that the photoactive surface of TiO_2 can be reached mainly by water resulting, after activation by UV light, in the production of large quantities of $OH^{\bullet}$ radicals. These can be released in the external solution being responsible for the degradation of paracetamol to *p*-aminophenol and finally to dicarboxylic acids, following the mechanisms previously proposed for the photocatalytic degradation of this molecule.[74] Increasing the amount of TiO_2 in the nanocomposite materials, some TiO_2 is present also outside the pores of the MSN support. In this case, the outermost surface of the material is mostly available for the photocatalytic reactions. Therefore, the initial rate of degradation of paracetamol is very high but the adsorption of intermediate compounds that can be produced by the partial decomposition of paracetamol by reaction with $OH^{\bullet}$ radicals could hindered the surface to following degradation reactions. Notably, positively charged (NH_4^+) or basic compounds (*p*-aminophenol) are present among the by-products of paracetamol decomposition. The deactivation by adsorption of the intermediates on the surface of the materials is suggested by the low intensities of the bands related to *p*-aminophenol and dicarboxylic acids in solution. The degradation rate of paracetamol remains low for a certain period (from 30 to 90 – 120 min of reaction). During this time, an equilibrium should take place between the degradation of the molecules adsorbed on the surface, the production of $OH^{\bullet}$ radicals on the free photocatalytic sites and the adsorption of the new intermediate formed. Once a certain amount of the intermediates is fully degraded and removed from the surface, the rate of paracetamol degradation increases again (after 90 – 120 min of irradiation) until the complete mineralization of the molecules is obtained.

On the basis of the degradation experiments presented in Figure 9, the 20TiO_2-MSN material has been selected for the reusability test. The results of the four consecutive experiments are presented in Figure S8. Although paracetamol is always completely degraded after 4h of irradiation, a progressive loss of performance was observed in the central part of the degradation experiments. In agreement with the considerations previously reported for the materials with higher TiO_2, loading, also in this case the decrease in the paracetamol degradation rate observed during the reusability test can be ascribed to the interference of the inorganic by-products produced during the previous experiment: the adsorption of by-products as nitrates could hinder the formation of $OH^{\bullet}$ while the adsorption of ammonium ions or carboxylate molecules (formiates, acetates, oxalates) could be oxidized instead of paracetamol itself. Moreover, it must be underlined that the initial concentration of paracetamol is higher than that employed during degradation of MB and MO. Therefore, also the concentration of inorganic by-products is higher, finally leading to a deeper deactivation.

Conclusions

In summary, nanocomposite materials based on pure anatase TiO_2 nanoparticles confined inside the channels of ordered mesoporous silica nanospheres, with very high surface area and narrow pore size distribution centred at 4.3 nm, have been synthesized. The TiO_2-SiO_2 composites, containing 10 wt.%, 20 wt.%, 30% and 40 wt.% of TiO_2, were obtained by the reaction of MSNs and titanium isopropoxide as titanium source.

XPS results and TEM micrographs suggest that a critical threshold in the TiO_2 loading exist between 20 and 30 wt%: below this threshold, the growth of TiO_2 crystallites takes place in the constricted space of the mesopores of MSNs, keeping their sizes within the silica pore diameters; when amount of TiO_2 exceeds this threshold, the growth of TiO_2 occurs also on the external surface of the silica network. For the samples with the lower TiO_2 content, a strong interaction between the two components of the materials, as evidenced by XPS measurements. The results from photocatalytic degradation of pollutant compounds suggest that xTiO_2-MSN catalysts provide a good combination of potential adsorptive and photocatalytic properties. The role of the two components seems to be complementary to obtain good performances in water remediation.

In MB degradation, mesoporous SiO_2 nanospheres adsorb the cationic dye while the anatase TiO_2 nanocrystals provide the photoactive sites for the dye degradation. In particular, the high activity demonstrated by 30TiO_2-MSN could be rationalized considering that this composition presents TiO_2 nanoparticles mainly located inside the MSN pores, with a small fraction decorating the surface of MSN.

In MO and paracetamol degradation, the adsorption of the target molecules on TiO_2 inside the pores of the MSN support is limited by the diffusion. This results in the protection of the photoactive material with respect to the adsorption of large amounts of organic compounds (target molecules or by-products of their partial degradation). Increasing the amount of TiO_2, some photoactive material is present in the external surface of the SiO_2 nanospheres, being more easily deactivated by adsorption of by-

products.

Finally, also considering the low amount of titania loaded, this type of nanocomposites could offer a simply way to tune the nanoarchitecture of a material, controlling the size and dispersion of the active phase present in the system, thus improving the catalytic behavior.

Acknowledgements

The authors acknowledge Mrs. Martina Marchiori for nitrogen physisorption analyses, Mr. Tiziano Finotto for XRD measurements, Dr. Luca Samiolo for DRUV-vis analyses and Prof. Paolo Fornasiero and Prof. Mauro Graziani for the helpful discussion.

TM and VG acknowledge support through the project FRA 2013. Universities of Venice, Trieste and Málaga, ICCOM-CNR and Consortium INSTM are acknowledged for financial support.

Notes and references

[a] *Department of Molecular Sciences and Nanosystems, Ca' Foscari University of Venice, INSTM Venice Research Unit, Via Torino 155/B, 30172 Mestre Venezia, Italy. Fax: +39-0412346735; Tel: +39-0412346745; E-mail: elisa.moretti@unive.it*

[b] *Centro di Microscopia Elettronica "Giovanni Stevanato", Ca' Foscari University of Venice, Italy.*

[c] *CSGI, Unit of Venice, Italy.*

[d] *Department of Chemical and Pharmaceutical Sciences, University of Trieste, ICCOM-CNR Trieste Research Unit and INSTM Trieste Research Unit, Via L. Giorgieri 1, 34127 Trieste, Italy.*

[e] *Departamento de Química Inorgánica, Cristalografía y Mineralogía, Facultad de Ciencias, Universidad de Málaga, Campus de Teatinos, E-29071 Málaga, Spain.*

† Electronic Supplementary Information (ESI) available: TEM micrographs at different magnification; deconvolution of the O 1s spectra for the $10TiO_2$-MSN sample; UV-vis spectra of the solutions recovered during photocatalytic degradaton of MB, MO and paracetamol; results from consecutive degradation experiments. See DOI: 10.1039/b000000x/

1. O. Carp, *Prog. Solid State Chem.*, 2004, **32**, 33–177.
2. J. Augustynski, *Electrochim. Acta*, 1993, **38**, 43–46.
3. K. K. Akurati, S. S. Bhattacharya, M. Winterer, and H. Hahn, *J. Phys. D. Appl. Phys.*, 2006, **39**, 2248–2254.
4. E. Pelizzetti, C. Minero, E. Borgarello, L. Tinucci, and N. Serpone, *Langmuir*, 1993, **9**, 2995–3001.
5. R. Campostrini, G. Carturan, L. Palmisano, M. Schiavello, and A. Sclafani, *Mater. Chem. Phys.*, 1994, **38**, 277–283.
6. J. Ovenstone, *J. Mater. Sci.*, 2001, **36**, 1325–1329.
7. M. Inagaki, Y. Nakazawa, M. Hirano, Y. Kobayashi, and M. Toyoda, *Int. J. Inorg. Mater.*, 2001, **3**, 809–811.
8. R. Rahal, A. Wankhade, D. Cha, A. Fihri, S. Ould-Chikh, U. Patil, and V. Polshettiwar, *RSC Adv.*, 2012, **2**, 7048.
9. C.-S. Kim, B. K. Moon, J.-H. Park, S. Tae Chung, and S.-M. Son, *J. Cryst. Growth*, 2003, **254**, 405–410.
10. W.-J. Ong, L.-L. Tan, S.-P. Chai, S.-T. Yong, and A. R. Mohamed, *Nanoscale*, 2014, **6**, 1946–2008.
11. Y. Luan, L. Jing, J. Wu, M. Xie, and Y. Feng, *Appl. Catal. B Environ.*, 2014, **147**, 29–34.
12. U. Diebold, *Surf. Sci. Rep.*, 2003, **48**, 53–229.
13. A. Fujishima, X. Zhang, and D. Tryk, *Surf. Sci. Rep.*, 2008, **63**, 515–582.
14. Y. Xu and C. H. Langford, *J. Phys. Chem.*, 1995, **99**, 11501–11507.
15. C. Anderson and A. J. Bard, *J. Phys. Chem. B*, 1997, **101**, 2611–2616.
16. J. Zhao, T. Wu, K. Wu, K. Oikawa, H. Hidaka, and N. Serpone, *Environ. Sci. Technol.*, 1998, **32**, 2394–2400.
17. Q. Wang, C. Chen, D. Zhao, W. Ma, and J. Zhao, *Langmuir*, 2008, **24**, 7338–45.
18. X. Chen and S. S. Mao, *Chem. Rev.*, 2007, **107**, 2891–959.
19. S. G. Kumar and L. G. Devi, *J. Phys. Chem. A*, 2011, **115**, 13211–41.
20. X. Wang, Z. Li, J. Shi, and Y. Yu, *Chem. Rev.*, 2014.
21. L. Wu, B. X. Yang, X. H. Yang, Z. G. Chen, Z. Li, H. J. Zhao, X. Q. Gong, and H. G. Yang, *CrystEngComm*, 2013, **15**, 3252.
22. C. Liu, X. Han, S. Xie, Q. Kuang, X. Wang, M. Jin, Z. Xie, and L. Zheng, *Chem. Asian J.*, 2013, **8**, 282–9.
23. H. G. Yang, C. H. Sun, S. Z. Qiao, J. Zou, G. Liu, S. C. Smith, H. M. Cheng, and G. Q. Lu, *Nature*, 2008, **453**, 638–41.
24. J. Pan, G. Liu, G. Q. M. Lu, and H.-M. Cheng, *Angew. Chem. Int. Ed. Engl.*, 2011, **50**, 2133–7.
25. J. Li and D. Xu, *Chem. Commun.*, 2010, **46**, 2301.
26. T. Ohno, K. Sarukawa, and M. Matsumura, *New J. Chem.*, 2002, **26**, 1167–1170.
27. T. R. Gordon, M. Cargnello, T. Paik, F. Mangolini, R. T. Weber, P. Fornasiero, and C. B. Murray, *J. Am. Chem. Soc.*, 2012, **134**, 6751–61.
28. H. Lin, L. Li, M. Zhao, X. Huang, X. Chen, G. Li, and R. Yu, *J. Am. Chem. Soc.*, 2012, **134**, 8328–31.
29. T. Ohno, T. Higo, N. Murakami, H. Saito, Q. Zhang, Y. Yang, and T. Tsubota, *Appl. Catal. B Environ.*, 2014, **152-153**, 309–316.
30. A.-W. Xu, Y. Gao, and H.-Q. Liu, *J. Catal.*, 2002, **207**, 151–157.
31. K. Nagaveni, M. S. Hegde, and G. Madras, *J. Phys. Chem. B*, 2004, **108**, 20204–20212.
32. J. Zhu, W. Zheng, B. He, J. Zhang, and M. Anpo, *J. Mol. Catal. A Chem.*, 2004, **216**, 35–43.
33. W. Choi, A. Termin, and M. R. Hoffmann, *J. Phys. Chem.*, 1994, **98**, 13669–13679.
34. A. Naldoni, M. Allieta, S. Santangelo, M. Marelli, F. Fabbri, S. Cappelli, C. L. Bianchi, R. Psaro, and V. Dal Santo, *J. Am. Chem. Soc.*, 2012, **134**, 7600–3.
35. K. C. Christoforidis, S. J. A. Figueroa, and M. Fernández-García, *Appl. Catal. B Environ.*, 2012, **117-118**, 310–316.
36. T. Ohno, M. Akiyoshi, T. Umebayashi, K. Asai, T. Mitsui, and M. Matsumura, *Appl. Catal. A Gen.*, 2004, **265**, 115–121.
37. W. Ren, Z. Ai, F. Jia, L. Zhang, X. Fan, and Z. Zou, *Appl. Catal. B Environ.*, 2007, **69**, 138–144.
38. J. W. J. Hamilton, J. A. Byrne, P. S. M. Dunlop, D. D. Dionysiou, M. Pelaez, K. O'Shea, D. Synnott, and S. C. Pillai, *J. Phys. Chem. C*, 2014, **118**, 12206–12215.
39. M. Fittipaldi, V. Gombac, A. Gasparotto, C. Deiana, G. Adami, D. Barreca, T. Montini, G. Martra, D. Gatteschi, and P. Fornasiero, *Chemphyschem*, 2011, **12**, 2221–4.
40. V. Gombac, L. De Rogatis, A. Gasparotto, G. Vicario, T. Montini, D. Barreca, G. Balducci, P. Fornasiero, E. Tondello, and M. Graziani, *Chem. Phys.*, 2007, **339**, 111–123.
41. V. Subramanian, E. Wolf, and P. V. Kamat, *J. Phys. Chem. B*, 2001, **105**, 11439–11446.
42. T. Montini, V. Gombac, L. Sordelli, J. J. Delgado, X. Chen, G. Adami, and P. Fornasiero, *ChemCatChem*, 2011, **3**, 574–577.
43. A. Gallo, T. Montini, M. Marelli, A. Minguzzi, V. Gombac, R. Psaro, P. Fornasiero, and V. Dal Santo, *ChemSusChem*, 2012, **5**, 1800–11.
44. B. Cheng, Y. Le, and J. Yu, *J. Hazard. Mater.*, 2010, **177**, 971–7.
45. R. S. Sonawane and M. K. Dongare, *J. Mol. Catal. A Chem.*, 2006, **243**, 68–76.
46. G. Li, L. Wu, F. Li, P. Xu, D. Zhang, and H. Li, *Nanoscale*, 2013, **5**, 2118–25.
47. B. Jiang, X. Yang, X. Li, D. Zhang, J. Zhu, and G. Li, *J. Sol-Gel Sci. Technol.*, 2013, **66**, 504–511.
48. Q. Zhang, W. Fan, and L. Gao, *Appl. Catal. B Environ.*, 2007, **76**, 168–173.
49. L. Lin, Y. Yang, L. Men, X. Wang, D. He, Y. Chai, B. Zhao, S. Ghoshroy, and Q. Tang, *Nanoscale*, 2013, **5**, 588–93.
50. D. Shchukin, S. Poznyak, A. Kulak, and P. Pichat, *J. Photochem. Photobiol. A Chem.*, 2004, **162**, 423–430.
51. A. I. Kontos, V. Likodimos, T. Stergiopoulos, D. S. Tsoukleris, P. Falaras, I. Rabias, G. Papavassiliou, D. Kim, J. Kunze, and P. Schmuki, *Chem. Mater.*, 2009, **21**, 662–672.
52. A. K. L. Sajjad, S. Shamaila, B. Tian, F. Chen, and J. Zhang, *J. Hazard. Mater.*, 2010, **177**, 781–91.

53. V. Puddu, R. Mokaya, and G. Li Puma, *Chem. Commun. (Camb).*, 2007, 4749–51.
54. P. Gao, A. Li, D. D. Sun, and W. J. Ng, *J. Hazard. Mater.*, 2014, **279C**, 96–104.
55. X. Yang, J. Qin, Y. Li, R. Zhang, and H. Tang, *J. Hazard. Mater.*, 2013, **261**, 342–50.
56. Y. H. Ng, I. V. Lightcap, K. Goodwin, M. Matsumura, and P. V. Kamat, *J. Phys. Chem. Lett.*, 2010, **1**, 2222–2227.
57. W. Dong, C. W. Lee, X. Lu, Y. Sun, W. Hua, G. Zhuang, S. Zhang, J. Chen, H. Hou, and D. Zhao, *Appl. Catal. B Environ.*, 2010, **95**, 197–207.
58. Z. Sun, Y. Chen, Q. Ke, Y. Yang, and J. Yuan, *J. Photochem. Photobiol. A Chem.*, 2002, **149**, 169–174.
59. V. Belessi, D. Lambropoulou, I. Konstantinou, A. Katsoulidis, P. Pomonis, D. Petridis, and T. Albanis, *Appl. Catal. B Environ.*, 2007, **73**, 292–299.
60. C. Anderson and A. J. Bard, *J. Phys. Chem.*, 1995, **99**, 9882–9885.
61. D. Papoulis, S. Komarneni, D. Panagiotaras, E. Stathatos, K. C. Christoforidis, M. Fernández-García, H. Li, Y. Shu, T. Sato, and H. Katsuki, *Appl. Catal. B Environ.*, 2014, **147**, 526–533.
62. E. Moretti, A. Talon, L. Storaro, A. Le Donne, S. Binetti, A. Benedetti, and S. Polizzi, *J. Lumin.*, 2014, **146**, 178–185.
63. S.-H. Wu, C.-Y. Mou, and H.-P. Lin, *Chem. Soc. Rev.*, 2013, **42**, 3862–75.
64. I. I. Slowing, J. L. Vivero-Escoto, B. G. Trewyn, and V. S.-Y. Lin, *J. Mater. Chem.*, 2010, **20**, 7924.
65. G. Sponchia, R. Marin, I. Freris, M. Marchiori, E. Moretti, L. Storaro, P. Canton, A. Lausi, A. Benedetti, and P. Riello, *J. Nanoparticle Res.*, 2014, **16**, 2245.
66. F. Hoffmann, M. Cornelius, J. Morell, and M. Fröba, *Angew. Chem. Int. Ed. Engl.*, 2006, **45**, 3216–51.
67. M. Lenarda, G. Chessa, E. Moretti, S. Polizzi, L. Storaro, and A. Talon, *J. Mater. Sci.*, 2006, **41**, 6305–6312.
68. S. Ma, Y. Wang, and Y. Zhu, *J. Porous Mater.*, 2010, **18**, 233–239.
69. N. B. Lihitkar, M. K. Abyaneh, V. Samuel, R. Pasricha, S. W. Gosavi, and S. K. Kulkarni, *J. Colloid Interface Sci.*, 2007, **314**, 310–6.
70. H. Lachheb, E. Puzenat, A. Houas, M. Ksibi, E. Elaloui, C. Guillard, and J.-M. Herrmann, *Appl. Catal. B Environ.*, 2002, **39**, 75–90.
71. C. Baiocchi, M. C. Brussino, E. Pramauro, A. B. Prevot, L. Palmisano, and G. Marcì, *Int. J. Mass Spectrom.*, 2002, **214**, 247–256.
72. A. Houas, H. Lachheb, M. Ksibi, E. Elaloui, C. Guillard, and J.-M. Herrmann, *Appl. Catal. B Environ.*, 2001, **31**, 145–157.
73. E. Moctezuma, E. Leyva, C. A. Aguilar, R. A. Luna, and C. Montalvo, *J. Hazard. Mater.*, 2012, **243**, 130–8.
74. L. Yang, L. E. Yu, and M. B. Ray, *Environ. Sci. Technol.*, 2009, **43**, 460–465.
75. Y. He, F. Grieser, and M. Ashokkumar, *Ultrason. Sonochem.*, 2011, **18**, 974–80.
76. K. Sing, D. Everett, R. Haul, L. Moscou, R. Pierotti, J. Rouquerol, and T. Siemieniewska, *Pure Appl Chem*, 1985, **57**, 603–619.
77. L. Zhao and J. Yu, *J. Colloid Interface Sci.*, 2006, **304**, 84–91.
78. S. Enzo, G. Fagherazzi, a. Benedetti, and S. Polizzi, *J. Appl. Crystallogr.*, 1988, **21**, 536–542.
79. J. Zhang, X. Liu, S. Wang, S. Wu, B. Cao, and S. Zheng, *Powder Technol.*, 2012, **217**, 585–590.
80. J. F. Moulder, W. F. Stickle, P. E. Sobol, and K. D. Bomben, *Handbook of X-ray Photoelectron Spectroscopy Edited by*, Perkin-Elmer Corporation, 1992.
81. N. Guo, Y. Liang, S. Lan, L. Liu, G. Ji, S. Gan, H. Zou, and X. Xu, *Appl. Surf. Sci.*, 2014, **305**, 562–574.
82. T. Ohno, K. Numakura, H. Itoh, H. Suzuki, and T. Matsuda, *Adv. Powder Technol.*, 2011, **22**, 390–395.
83. M. Vishwas, K. N. Rao, K. V Arjuna Gowda, and R. P. S. Chakradhar, *Spectrochim. Acta. A. Mol. Biomol. Spectrosc.*, 2011, **83**, 614–7.
84. J. Yang, J. Zhang, L. Zhu, S. Chen, Y. Zhang, Y. Tang, Y. Zhu, and Y. Li, *J. Hazard. Mater.*, 2006, **137**, 952–8.
85. F. E. Osterloh, *Chem. Soc. Rev.*, 2013, **42**, 2294–320.
86. J. Marugán, M.-J. M.-J. López-Muñoz, R. van Grieken, and J. Aguado, *Ind. Eng. Chem. Res.*, 2007, **46**, 7605–7610.
87. K. Balachandran, R. Venckatesh, R. Sivaraj, and P. Rajiv, *Spectrochim. Acta. A. Mol. Biomol. Spectrosc.*, 2014, **128**, 468–74.
88. D. Arun Kumar, J. Alex Xavier, J. Merline Shyla, and F. P. Xavier, *J. Mater. Sci.*, 2013, **48**, 3700–3707.
89. T. Ohno, S. Tagawa, H. Itoh, H. Suzuki, and T. Matsuda, *Mater. Chem. Phys.*, 2009, **113**, 119–123.
90. T. M. R. Viseu, B. Almeida, M. Stchakovsky, B. Drevillon, M. I. C. Ferreira, and J. B. Sousa, *Thin Solid Films*, 2001, **401**, 216–224.
91. W. Dong, Y. Sun, W. L. Chul, W. Hua, X. Lu, Y. Shi, S. Zhang, J. Chen, and D. Zhao, *J. Am. Chem. Soc.*, 2007, **129**, 13894–13904.
92. W. Dong, Y. Sun, Q. Ma, L. Zhu, W. Hua, X. Lu, G. Zhuang, S. Zhang, Z. Guo, and D. Zhao, *J. Hazard. Mater.*, 2012, **229-230**, 307–20.
93. G. K. C. Low, S. R. McEvoy, and R. W. Matthews, *Environ. Sci. Technol.*, 1991, **25**, 460–467.
94. K. Nohara, H. Hidaka, E. Pelizzetti, and N. Serpone, *J. Photochem. Photobiol. A Chem.*, 1997, **102**, 265–272.
95. E. Beyers, E. Biermans, S. Ribbens, K. De Witte, M. Mertens, V. Meynen, S. Bals, G. Van Tendeloo, E. F. Vansant, and P. Cool, *Appl. Catal. B Environ.*, 2009, **88**, 515–524.
96. M. Kosmulski, *Adv. Colloid Interface Sci.*, 2009, **152**, 14–25.
97. M. Stylidi, *Appl. Catal. B Environ.*, 2003, **40**, 271–286.